EDGE ARTICLE

Check for updates

Supramolecular interaction of a molecular catalyst with a polymeric carbon nitride photoanode enhances photoelectrochemical activity and stability at neutral pH†

Sanjit Mondal,‡[a] Martina Salati, ‡[bc] Marco Nicaso,[bc] Josep Albero, [d] Mireia Segado-Centellas, [b] Michael Volokh, [a] Carles Bo, *[b] Hermenegildo García, [d] Marcos Gil-Sepulcre,*[b] Antoni Llobet *[be] and Menny Shalom *[a]

Polymeric carbon nitride (CN) emerged as an alternative, metal-free photoanode material for water-splitting photoelectrochemical cells (PECs). However, the performance of CN photoanodes is limited due to the slow charge separation and water oxidation kinetics due to poor interaction with water oxidation catalysts (WOCs). Moreover, operation under benign, neutral pH conditions is rarely reported. Here, we design a porous CN photoanode connected to a highly active molecular Ru-based WOC, which also acts as an additional photo-absorber. We show that the strong interaction between the π-system of the heptazine units within the CN with the CH groups of the WOC's equatorial ligand enables a strong connection between them and an efficient electronic communication path. The optimized photoanode exhibits a photocurrent density of 180 ± 10 μA cm^{-2} at 1.23 V *vs.* the reversible hydrogen electrode (RHE) with 89% faradaic efficiency for oxygen evolution with turnover numbers (TONs) in the range of 3300 and a turnover frequency (TOF) of 0.4 s^{-1}, low onset potential, extended incident photon to current conversion, and good stability up to 5 h. This study may lead to the integration of molecular catalysts and polymeric organic absorbers using supramolecular interactions.

Introduction

Polymeric carbon nitride (CN) has gained significant interest as a low-cost and benign photoanodic material for water-splitting photoelectrochemical cells (PECs).[1–7] However, low charge separation and transfer efficiency and slow water oxidation kinetics hinder the photoactivity and PEC performance of CN

aDepartment of Chemistry and Ilse Katz Institute for Nanoscale Science and Technology, Ben-Gurion University of the Negev, Beer-Sheva 8410501, Israel. E-mail: mennysh@bgu.ac.il

bInstitute of Chemical Research of Catalonia (ICIQ), Barcelona Institute of Science and Technology (BIST), Av. Països Catalans 16, Tarragona 43007, Spain. E-mail: cbo@iciq.cat; mgil@iciq.cat; allobet@iciq.cat

cUniversitat Rovira i Virgili, Av. Països Catalans 35, Tarragona 43007, Spain

dInstituto de Tecnología Química CSIC-UPV, Universitat Politècnica de València, València 46022, Spain

eDepartament de Química, Universitat Autònoma de Barcelona Cerdanyola del Valles, Barcelona 08193, Spain

photoanodes.[8–12] Moreover, a pristine CN photoanode is prone to degradation due to the moderate oxygen evolution reaction (OER), which leads to hole accumulation and self-oxidation of the CN layer.[8,13,14] Therefore, low faradaic efficiencies (FEs) towards molecular oxygen and poor stability are usually observed. A common approach to overcoming the sluggish OER kinetics in PECs is introducing a co-catalyst, which acts as a hole sink and catalytic site for the OER.[15] In recent years, only a few reports have shown that heterogeneous metal oxide-based co-catalysts can improve the CN photoanode activity towards the OER.[15–18] Unlike metal oxide-based photoanodes (BiVO$_4$ and Fe$_2$O$_3$), most known co-catalyst deposition methods did not lead to enhanced oxygen production on a CN-based photoanode.[19–24] The poor hole transfer from the CN to the co-catalyst may stem from the insufficient interaction between the materials, although it is still not fully understood. Moreover, CN and many heterogeneous OER electrocatalysts based on oxides work efficiently only under alkaline conditions.[8,15] Consequently, the performance of CN photoanodes in a neutral electrolyte medium is relatively poor.[25,26] There is an allure in achieving a water-splitting PEC under neutral conditions as it offers gentler operating conditions than alkaline or acidic environments.

High performance and robust molecular catalysts have been developed recently for the water oxidation reaction, mainly based on Ru complexes containing the so-called FAME (flexible, adaptable, multidentate, and equatorial) ligands that achieve high turnover numbers (TONs) and turnover frequencies (TOFs), with $[Ru^{II}(tda-\kappa-N^3O)(py)_2]$ (Ru-tda, where tda^{2-} is [2,2′:6′,2″-terpyridine]-6,6″-dicarboxylate and py is pyridine) being one of the best examples.[27–29] The well-defined nature of these molecular catalysts, together with the capacity to spectroscopically characterize intermediates, has prompted a remarkable development of water oxidation catalysts (WOCs).[30] In addition, the capacity to functionalize the ligands bonding to the metal center offers a wide variety of anchoring strategies.[31–35] Recently, we have developed an oligomeric derivative of Ru-tda catalysts, using 4,4′-bpy as the bridging ligand to form $[Ru(tda)(4,4′-bpy)]_{15}(4,4′-bpy)$ (**Ru$_{15}$**).[34] The latter has the capacity to generate a large number of CH–π interactions with graphitic surfaces, generating robust hybrid materials for the efficient oxidation of water in a heterogeneous phase.

In the present work, we explore the capacity of the **Ru$_{15}$** catalyst to interact with the π system of heptazines, constituting the repeating unit of the CN material, via the CH groups of the tda ligand and generating a monolayer of the well-defined molecular catalyst on top of the CN surface. The CN synthetic procedure is chosen to form a porous layer with good adhesion to the conductive substrate (i.e., fluorine-doped tin oxide, FTO), allowing the exploration of the co-catalyst role in an FTO/CN/**Ru$_{15}$** photoanode. This should provide the needed electronic communication between the co-catalyst and the light absorbing material, leading to a superior performance of the hybrid material constituted by **Ru$_{15}$** and CN.
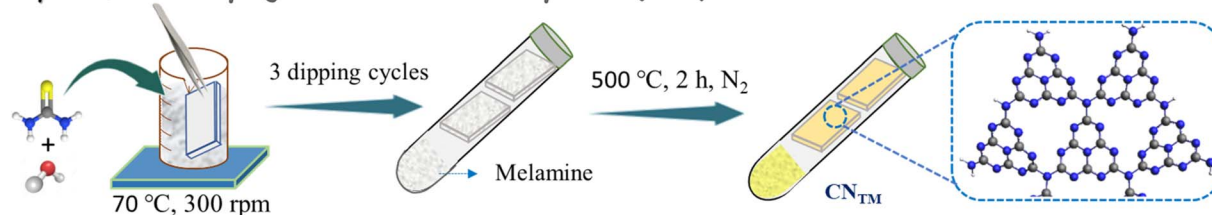
Results and discussion

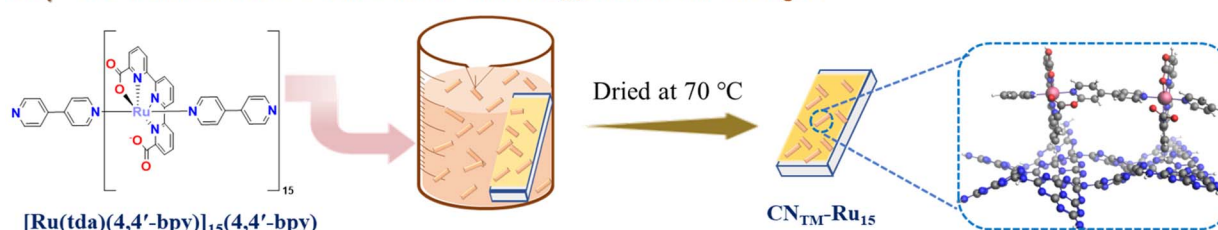The fabrication process of a porous CN film over FTO-coated glass as the substrate is illustrated in Scheme 1. Thiourea and melamine were used to prepare **CN$_{TM}$** photoanodes using a two-step method involving dipping and thermal treatment. The anchoring of the **Ru$_{15}$** oligomer into the **CN$_{TM}$** film was performed by dipping the **CN$_{TM}$** electrode in a solution containing 1 mg of **Ru$_{15}$** in 10 mL of 2,2,2-trifluoroethanol (TFE), for 20 min. Afterward, the electrode was removed from the solution and rinsed with TFE to generate the hybrid material, **CN$_{TM}$–Ru$_{15}$**. Further experimental details are given in the ESI.† The interaction of the **Ru$_{15}$** oligomeric water oxidation catalyst with the surface of the CN film occurs via CH–π interaction, as we have previously described in the case of graphitic surfaces.[34–36] In order to further characterize this interaction and visualize it, we have carried out DFT calculations with a low molecular weight model system that involves 10 heptazine units (164 atoms: 60 C, 86 N, and 18 H) for the carbon nitride, labelled as **CN$_{Red}$**, and a dinuclear Ru complex $\{[Ru(tda)(py)]_2(\mu-4,4′-bpy)\}$ labeled as **Ru$_2$**, to form **CN$_{Red}$–Ru$_2$** (see Fig. 1, S14–S22 and Tables S4–S7†). Structural combinations of the two units were explored, including aqueous solvent effects, yielding, in the most favorable case, a stabilization energy of 12.7 kcal mol^{-1} per Ru center, which would imply 190.5 kcal mol^{-1} for the entire **Ru$_{15}$** oligomer with **CN$_{TM}$**. This large stabilization energy is due to CH–π interactions between the CH aromatic groups of the tda ligands bonded to the Ru center and the π-system of the **CN$_{Red}$** surface.

XRD (X-ray diffraction) and FTIR (Fourier transform infrared) spectroscopy were used to investigate the structural and functional properties of the films. The **CN$_{TM}$** material exhibits two characteristic diffraction signals at 13.0° and 27.4°, which can be assigned to (100) and (002) planes, respectively, representative of the interplanar spacing and the conjugated aromatic system (Fig. 2a) in a heptazine-based CN.[37,38] Upon the incorporation of the **Ru$_{15}$** oligomeric catalyst, the XRD pattern remains unchanged, highlighting the structural stability of **CN$_{TM}$** films. The FTIR spectra of **CN$_{TM}$** and **CN$_{TM}$–Ru$_{15}$** films show a typical peak at 805 cm^{-1}, which corresponds to the breathing mode of triazine units present in the sample (Fig. 2b).

Scheme 1 Procedure for the preparation of a **CN$_{TM}$** film and the anchoring of the **Ru$_{15}$** oligomer to generate the hybrid material **CN$_{TM}$–Ru$_{15}$**.

In the scheme:

Step-I: Growth of polymeric carbon nitride porous (PCN) film over an FTO substrate

3 dipping cycles — 70 °C, 300 rpm — Melamine — 500 °C, 2 h, N$_2$ — **CN$_{TM}$**

Step-II: Modification of PCN surface with Ru$_{15}$ molecular catalyst

[Ru(tda)(4,4′-bpy)]$_{15}$(4,4′-bpy) — Dried at 70 °C — **CN$_{TM}$-Ru$_{15}$**

Fig. 1 (a) Side and (b) top views of the DFT calculated model of $CN_{Red}-Ru_2$. (c) Top and (d) side views of the optimized structure consisting of two layers of heptazine units $(CN_{Red})_2$ interacting *via* $\pi-\pi$ stacking interactions. (e) Density of states diagram for $(CN_{Red})_2$.
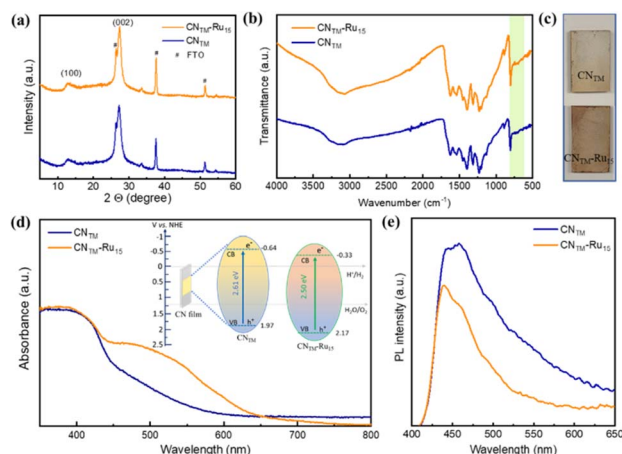

Fig. 2 (a) XRD of CN_{TM} and $CN_{TM}-Ru_{15}$ films over FTO-coated glass. (b) FTIR spectra of CN_{TM} and $CN_{TM}-Ru_{15}$ films. Spectra are vertically offset for clarity. (c) Digital photographs of CN_{TM} and $CN_{TM}-Ru_{15}$ photoelectrodes on FTO. (d) UV-vis DRS of CN_{TM} and $CN_{TM}-Ru_{15}$ films. Inset shows the schematic representation of the electronic band structure of CN_{TM} and $CN_{TM}-Ru_{15}$ (on the normal hydrogen electrode (NHE) scale) determined using the XPS-VB position and the optical E_g calculation. (e) Photoluminescence emission spectra (excitation wavelength: 370 nm) of CN_{TM} and $CN_{TM}-Ru_{15}$ films.

Additionally, the stretching modes of CN heterocycles were observed between 1200 and 1600 cm^{-1}, with specific vibrations at 1400 and 1633 cm^{-1} in the CN_{TM} film. Upon loading of the Ru_{15} catalyst onto the CN_{TM} film, the stretching modes of the CN heterocycles are found at 1394 and 1625 cm^{-1}. The broad band observed between 2980 and 3500 cm^{-1} in the spectra is attributed to either NH$_2$ groups or surface-adsorbed water molecules.[38] Additionally, ^{1}H NMR, XRD, and FTIR data of the Ru_{15} oligomer are provided in Fig. S1.†

The modification of the CN_{TM} film with the Ru_{15} oligomer has caused a visual change in the electrodes (Fig. 2c), which translates into the presence of a new broad band at approximately 480–550 nm, associated with the metal to ligand charge transfer (MLCT) band for the Ru complex, as can be observed in the diffuse reflectance spectrum (DRS) in Fig. 2d, and is comparable to the one visible in the UV-vis spectrum of Ru_{15} (Fig. S2†).

The direct optical bandgaps (E_g) of the CN_{TM} and $CN_{TM}-Ru_{15}$ films are 2.61 and 2.50 eV, respectively (Fig. S3†). Valence band X-ray photoelectron spectroscopy (VB-XPS) discloses a more positive VB energy (E_{VB}) position for the $CN_{TM}-Ru_{15}$ films of 2.17 V *vs.* NHE with regard to that of bare CN_{TM}, which gives a value of 1.97 V *vs.* NHE and thus a better thermodynamic driving force for the former (Fig. S4†).[10,38] Finally, the corresponding conduction band energy (E_{CB}) of the CN_{TM} and $CN_{TM}-Ru_{15}$ films is -0.64 and -0.33 V *vs.* NHE, respectively (see the inset of Fig. 2d for the energy diagram).

The electronic properties of the CN_{TM} material were also analyzed based on TD-DFT calculations. A single sheet of CN_{Red} made out of 10 heptazine units gave a band gap of 3.25 eV. Interestingly, a two-layer structure of heptazine units $(CN_{Red})_2$ interacting *via* $\pi-\pi$ stacking, as shown in Fig. 1, has a band gap of 2.62 eV closely matching the experimental value (2.61 eV), thus manifesting the importance of the delocalization of the electron density on the 2D network along with the $\pi-\pi$ stacking interactions among the different layers to properly describe carbon nitride type materials.

Photoluminescence (PL) spectra are significantly different in the presence and absence of Ru_{15}, as can be observed in Fig. 2e, where the intensity of the prominent emission peak at 450 nm in $CN_{TM}-Ru_{15}$ is partially quenched compared to pristine CN_{TM}, suggesting the presence of an alternative non-radiative recombination path.[39,40]

The SEM images of CN_{TM} (Fig. 3a) indicate a porous sheet-like morphology with good adhesion to the FTO substrate with a thickness of 40–50 μm. The CN_{TM}–Ru_{15} film images (Fig. 3d–f) suggest the preservation of the porous sheet-like morphology, with a rough surface. Cross-section analysis (Fig. 3g and h) indicates an intimate contact between the film and substrate with film thickness similar to that of the CN_{TM} film. Energy dispersive X-ray spectroscopy (EDS) confirms the presence of Ru in the CN_{TM}–Ru_{15} film (Fig. S5†). Moreover, the morphology of the CN_{TM}–Ru_{15} sample was examined using a high-angle annular dark-field scanning transmission electron microscope (HAADF-STEM), revealing the layered structure of CN (see Fig. S6†). EDS mapping further confirms the presence and distribution of the Ru_{15} oligomer over the CN surface (Fig. S7†).

X-ray photoelectron spectroscopy (XPS) confirms the successful loading of Ru_{15} on the CN_{TM} film, showing the presence of C, N, and Ru in the CN_{TM}–Ru_{15} film (Fig. S8a†). The high-resolution XPS C 1s spectrum of the CN_{TM} film (Fig. S8b†) exhibits three peaks centered around 284.7 and 288.3 eV, assigned to C=O groups, sp^2 C–C bonding, and N–C=N

bonding in the triazine units of carbon nitride, respectively. The high-resolution N 1s XPS curve shows three deconvoluted peaks attributed to C–N=C, N–$(C)_3$, and C–N–H_x bonds, respectively (Fig. S8c†).[39,41,42] The deconvolution of the C 1s spectrum of the CN_{TM}–Ru_{15} sample reveals six peaks. The additional three peaks are ascribed to C–C=C (sp^2), $N(sp^2)$–C, and Ru $3d_{3/2}$ (overlapping with C 1s), respectively, originating from the Ru oligomer (Fig. S8b†). The N 1s spectrum of CN_{TM}–Ru_{15} shows five deconvoluted peaks, where two additional peaks are centered at 397.4 and 399.2 eV and originate from the Ru oligomer (Fig. S8c†). The high-resolution S 2p spectrum (Fig. S8d†) shows peaks centered at 167.9 and 169.6 eV, ascribed to an S–H bond (S $2p_{3/2}$ and S $2p_{1/2}$, respectively) in the CN film, which was prepared using a thiourea precursor as the S source.

It is noteworthy that the peaks related to C–N=C, N–$(C)_3$, and C–N–H_x bonds stemming from the carbon nitride have shifted to higher binding energies after modification with Ru_{15} due to the Ru oligomer/CN interaction. The high-resolution XPS Ru 3p spectrum of the CN_{TM}–Ru_{15} film displays peaks in the 485–460 eV range, attributed to the presence of Ru(II) species (Fig. 3i).[43] Finally, inductively coupled plasma optical emission
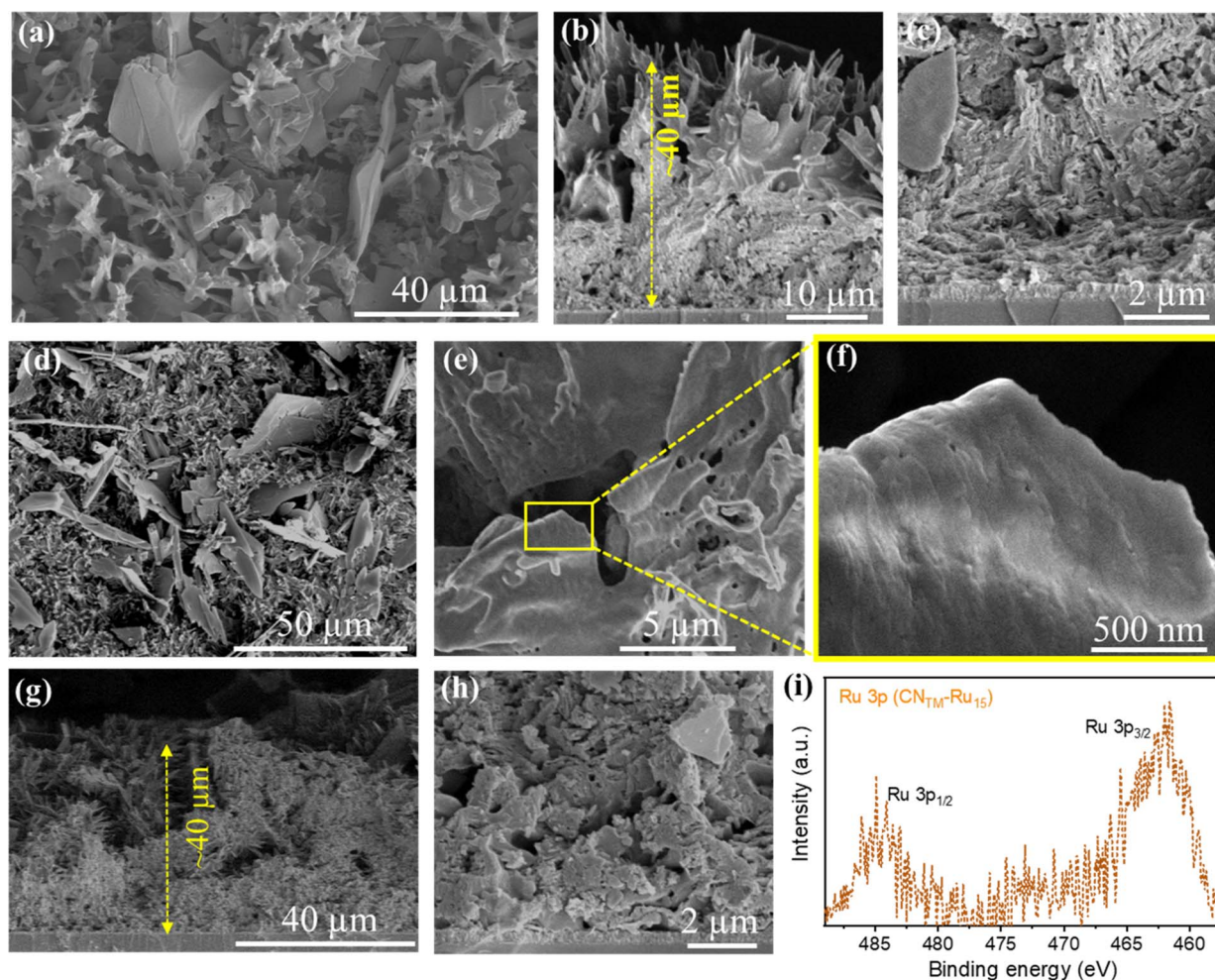

Fig. 3 (a) SEM image showing the morphology of the upper surface of the CN_{TM} electrode. (b and c) Cross-sectional SEM images of CN_{TM} electrodes at different magnifications. (d, e and f) Top views of CN_{TM}–Ru_{15} at different magnifications. (g and h) Cross-sectional SEM images of CN_{TM}–Ru_{15} electrodes at different magnifications. (i) High-resolution Ru 3p XPS spectrum of a CN_{TM}–Ru_{15} film.

spectroscopy (ICP-OES) elemental analysis for the $CN_{TM}-Ru_{15}$ samples gives 6.5 μg of Ru per g of sample, which implies 64.3 nmol of Ru per g of $CN_{TM}-Ru_{15}$ (see Table S1†).

PEC measurements of CN_{TM} and $CN_{TM}-Ru_{15}$ films were performed in a three-electrode system under simulated 1 sun illumination in a NaH_2PO_4/Na_2HPO_4 buffer solution (pH 7 and ionic strength 0.1 M) as a supporting electrolyte. The linear sweep voltammetry (LSV) curves (Fig. 4a) of CN_{TM} and $CN_{TM}-Ru_{15}$ films demonstrate a typical PEC behavior, with an onset potential of 0.55 V *vs.* RHE. Chronoamperometry measurements at 1.23 V *vs.* RHE (Fig. 4b) reveal that the incorporation of Ru_{15} leads to an improvement in the photocurrent densities of about 40%, from 130 ± 8 μA cm^{-2} for the CN_{TM} film to 180 ± 10 μA cm^{-2} for the $CN_{TM}-Ru_{15}$ film, both at an $E_{app} = 1.23$ V *vs.* RHE. This improvement is attributed to the synergy between the

CN_{TM} and Ru_{15} anchored on the surface by CH–π interactions, facilitating charge transfer and separation and the additional capacity of Ru_{15} to efficiently catalyze the water oxidation reaction.

The measured incident photon-to-current conversion efficiency (IPCE) of CN_{TM} and $CN_{TM}-Ru_{15}$ films at several illumination wavelengths ranging from 280 to 650 nm is displayed in Fig. 4c. The IPCE values are in good agreement with the absorption spectra of the films. The IPCE value of the $CN_{TM}-Ru_{15}$ film (6.7%) is higher than that of the CN_{TM} film (5.8%) at 370 nm. In addition, the IPCE measurement reveals that the $CN_{TM}-Ru_{15}$ film is photoactive at longer wavelengths, up to ~550 nm (inset of Fig. 4c), mainly due to the contribution of Ru_{15} (Fig. S2†).

Fig. 4 (a) Linear sweep voltammetry (LSV) of CN_{TM} and $CN_{TM}-Ru_{15}$ electrodes (phosphate buffer, pH 7) in the dark and under 1 sun illumination. (b) Chronoamperometry (current densities *vs.* time) of CN_{TM} and $CN_{TM}-Ru_{15}$ electrodes in phosphate buffer (pH 7) at 1.23 V_{RHE} upon on/off 1 sun illumination. (c) Incident photon-to-current conversion efficiency (IPCE) of the CN_{TM} and $CN_{TM}-Ru_{15}$ films at different wavelengths (280–650 nm) in a phosphate buffer solution (pH 7) at 1.23 V_{RHE}. (d) Stability measurement (current density under continuous 1 sun illumination) of CN_{TM} and $CN_{TM}-Ru_{15}$ electrodes in phosphate buffer (pH 7). (e) Nyquist plot of CN_{TM} and $CN_{TM}-Ru_{15}$ films (fitted data shown). As an inset, the equivalent circuit used for fitting is shown, including a Warburg diffusion element (W); the R_{ct} value was obtained by fitting the semicircles of the Nyquist plots. (f) Cathodic and anodic charging current densities of CN films at 0 V *vs.* Ag/AgCl as a function of scan rate. (g) Transient absorption spectra of CN_{TM} (blue triangles) and $CN_{TM}-Ru_{15}$ (orange hexagons) dispersions in MeCN acquired at 250 ns. (h) Transient absorption decays of CN_{TM} (blue) and $CN_{TM}-Ru_{15}$ (orange) dispersions in MeCN, monitored at 650 nm. The measurements were performed upon laser excitation at 355 nm under a N_2 atmosphere. The CN_{TM} and $CN_{TM}-Ru_{15}$ dispersions' UV-vis absorption was adjusted at identical values at the excitation wavelength (355 nm).
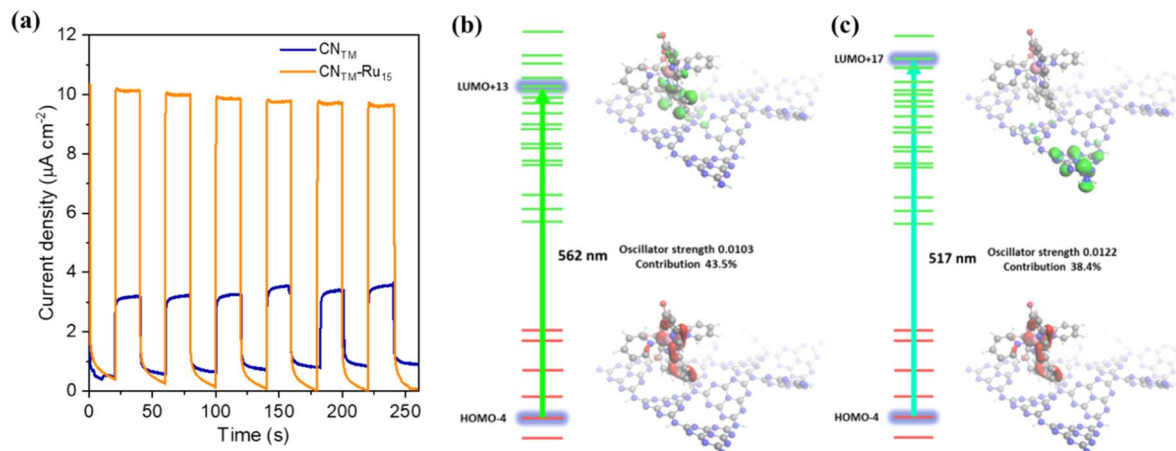
Fig. 5 (a) Chronoamperometry (current densities *vs.* time) of CN_{TM} and $CN_{TM}-Ru_{15}$ electrodes in phosphate buffer (pH 7) at 1.23 V *vs.* RHE under illumination using a 510 nm band-pass filter (FWHM 10 nm). (b and c) Calculated major contributions for electronic transition.

Notably, the incorporation of Ru_{15} into the CN_{TM} film significantly enhances the long-term stability. As shown in Fig. 4d, $CN_{TM}-Ru_{15}$ films in a neutral pH medium retain ~35% photocurrent density even after 5.5 h. In sharp contrast, the CN_{TM} film completely loses its photocurrent density (~96%) within 2 hours. Importantly, O_2 measurements indicate that most of the current is attributed to oxygen evolution and not to the self-oxidation of the CN layer. $CN_{TM}-Ru_{15}$ generates O_2 at a rate of 0.014 μmol cm^{-2} min^{-1} (Fig. S9†) with a faradaic efficiency (FE) of up to 89% after 20 min. Overall, this implies a TON over 3000 after 5 h and a TOF of 0.4 s^{-1} (Table S2†).

A comparison table for the PEC performance using metal oxides as WOC co-catalysts with a CN-based film is given in Table S3.† It is worth mentioning that the molecular hybrid material is superior in terms of FE for O_2 generation. It is also important to mention here that the amount of Ru used is in the range of micrograms of Ru per g of sample. This generally implies a loading of catalyst 4 to 6 orders of magnitude lower[34,35] than related examples using Co, Ni, or Fe oxides.[44,45]

The $CN_{TM}-Ru_{15}$ film after the stability experiment was examined using PXRD, XPS and SEM (Fig. S10†), revealing minimal alterations in the film's structure and morphology. The improved durability of the $CN_{TM}-Ru_{15}$ film is associated with better charge separation and the high OER catalytic activity of Ru_{15}. We analyzed the charge transfer kinetics behavior of CN_{TM} and $CN_{TM}-Ru_{15}$ films using electrochemical impedance spectroscopy (EIS) and transient absorption spectroscopy (TAS) to elucidate the activity improvement. The EIS experiments (Fig. 4e and S11†) disclosed lower charge transfer resistance (R_{ct} = 250 kΩ) for the $CN_{TM}-Ru_{15}$ film than for CN_{TM} alone (470 kΩ), implying better hole transfer to the solution. An increased electrochemically active surface area (ECSA) is shown in Fig. 4f and S12,† indicating more active sites for water oxidation after modification with the Ru_{15} oligomer.

TAS measurements of CN_{TM} and $CN_{TM}-Ru_{15}$ dispersions in MeCN upon 355 nm laser excitation further confirmed the improved photo-induced charge transfer kinetics in the presence of Ru_{15}. The TA spectrum of CN_{TM} (Fig. 4g) exhibits

a negative feature up to *ca.* 525 nm, due to the bleaching of the ground state absorption of CN_{TM}. The detected positive signal from 525 to 750 nm indicates the presence of excited states absorbing in the visible region, as previously reported for related CN materials. The TA spectrum of $CN_{TM}-Ru_{15}$ presents similar features with higher signal intensity. Still, it exhibits extended transient absorption in the NIR region (750–800 nm) due to the Ru_{15} incorporation. It is worth noticing that the increase in the positive signal intensity for $CN_{TM}-Ru_{15}$ is proportional to an enhancement in photo-induced charge carriers, in good agreement with the photocurrent and IPCE measurements, indicating a more efficient charge separation in $CN_{TM}-Ru_{15}$ compared to CN_{TM}. These positive signals are attributed to photo-generated electrons in CN_{TM} and $CN_{TM}-Ru_{15}$. Hole quenching experiments using MeOH as a sacrificial electron donor (Fig. S13†) confirm that the electrons are the main charge carriers detected under these experimental conditions.

The TA decays of CN_{TM} and $CN_{TM}-Ru_{15}$ at 650 nm (Fig. 4h) reveal an almost one magnitude order longer electron half-lifetime of $CN_{TM}-Ru_{15}$ (1.60 μs) *vs.* CN_{TM} (0.24 μs) thanks to a better charge separation and thus lower recombination rates. This agrees with the mechanism proposed in eqn (1)–(3):

$$[CN_{TM}-Ru_{15}] + h\nu \rightarrow [CN_{TM}-Ru_{15}]^* \text{ (excited state)} \quad (1)$$

$$[CN_{TM}-Ru_{15}]^* \rightarrow [^-CN_{TM}-Ru_{15}{}^+] \text{ (charge separated state)} \quad (2)$$

$$4[^-CN_{TM}-Ru_{15}{}^+] + 2H_2O \rightarrow$$
$$4[CN_{TM}-Ru_{15}] + O_2 + 4H^+ + 4e^- \text{ (WOR)} \quad (3)$$

where the introduction of supramolecularly bonded Ru_{15} on the CN_{TM} layer results in an enhanced charge separated state (eqn (2)), mainly thanks to fast hole extraction from CN_{TM} to Ru_{15}, followed by the water oxidation reaction (WOR) (eqn (3)). The final assembly thus overall leads to better photoactivity at longer wavelengths and better electron collection.

Furthermore, additional photocurrent measurements were performed using a 510 nm band-pass filter (FWHM 10 nm) for

both electrodes, as presented in Fig. 5a, showing a photocurrent enhancement of approx. 3.2 times higher in the case of CN_{TM}–Ru_{15} compared to CN_{TM} due to the presence of the molecular catalyst. This points out the behavior of Ru_{15} as both a light absorber and a catalyst.[46] To gain some insights into the processes occurring upon light excitation of the system, we computed the absorption spectra by means of TD-DFT of the model hybrid CN_{Red}–Ru_2, and the results are shown in Fig. 5 and S14–S22.† Two transitions are displayed in the figure, one at 562 nm (Fig. 5b) that is mainly intramolecular involving the Ru catalyst, which later on can further transfer an electron to the valence band of the CN_{Red} moiety, resembling the typical Grätzel's dye-sensitized solar cells based on TiO_2 and $[Ru(bpy)_3]^{2+}$.[47,48] A second excitation at 517 nm, shown in Fig. 5c, would involve a direct charge transfer from the Ru center to the valence band of CN_{Red}.

Conclusions

In this work, we introduced a new molecular hybrid material CN_{TM}–Ru_{15} based on the anchoring of a highly active molecular water oxidation catalyst on a CN_{TM} photoanode. The successful deposition of the Ru_{15} oligomer on polymeric carbon nitride photoanodes (CN_{TM}) through CH–π interactions enables good photoelectrochemical water-splitting activity at neutral pH, enhanced long-term stability and high FE (>89%) for oxygen production. Detailed structural, photoelectrochemical, and mechanistic studies reveal that Ru_{15} markedly improves charge separation and hole extraction kinetics, enabling efficient water oxidation. Furthermore, the Ru_{15} oligomer leads to better light harvesting, a higher electrochemical surface area, and improved electronic conductivity. The optimized CN_{TM}–Ru_{15} film demonstrates a photocurrent density of $180 \pm 10 \ \mu A \ cm^{-2}$ with 89% FE for oxygen evolution, good stability up to 5 h, and IPCE values up to 6.7%. The amount of Ru-based catalyst loaded on the surface represents only 6.5 ppm of the electrode composition and leads to TONs in the range of 3300 and a TOF of $0.4 \ s^{-1}$. Furthermore, we have also shown that in the CN_{TM}–Ru_{15} hybrid material, the Ru centers act both as a catalyst and as a photoabsorber.

Finally, the present work is an example of positive synergy that can be obtained with the proper utilization of a molecular-based catalyst and a polymeric organic absorber.

Data availability

The data supporting this article have been included as part of the ESI.† The underlying raw data are available on request from the authors.

Author contributions

S. M. performed most of the experiments, analyzed the data, and wrote the initial draft of the manuscript. M. S. synthesized and characterized the $Ru15$ oligomer and participated in manuscript writing. M. N. performed the DFT calculations and analysis. J. A. and H. G. performed the TAS measurements. M. S. C., C. B., and M. G. S. took part in the DFT study. M. V. took part in analysis, SEM imaging, and manuscript editing. M. S. and A. L. supervised the study, co-wrote and reviewed the paper, and acquired funding. All the authors discussed the results and reviewed the manuscript. All authors have given approval to the final version of the manuscript.

Conflicts of interest

There are no conflicts to declare.

Acknowledgements

References

1 M. Volokh, G. Peng, J. Barrio and M. Shalom, *Angew. Chem., Int. Ed.*, 2019, **58**, 6138–6151.

2 N. P. Dharmarajan, D. Vidyasagar, J.-H. Yang, S. N. Talapaneni, J. Lee, K. Ramadass, G. Singh, M. Fawaz, P. Kumar and A. Vinu, *Adv. Mater.*, 2023, **36**, 2306895.

3 X. Fan, Z. Wang, T. Lin, D. Du, M. Xiao, P. Chen, S. A. Monny, H. Huang, M. Lyu, M. Lu and L. Wang, *Angew. Chem., Int. Ed.*, 2022, **61**, e202204407.

4 G. Peng, J. Albero, H. Garcia and M. Shalom, *Angew. Chem., Int. Ed.*, 2018, **57**, 15807–15811.

5 J. Zhang, J. Zhang, C. Dong, Y. Xia, L. Jiang, G. Wang, R. Wang and J. Chen, *Small*, 2023, **19**, 2208049.

6 T. H. Jeon, C. Park, U. Kang, G. Moon, W. Kim, H. Park and W. Choi, *Appl. Catal., B*, 2024, **340**, 123167.

7 M. Fawaz, R. Bahadur, N. Panangattu Dharmarajan, J.-H. Yang, C. I. Sathish, A. M. Sadanandan,

V. Perumalsamy, G. Singh, X. Guan, P. Kumar and A. Vinu, *Carbon.*, 2023, **214**, 118345.

8 J. Qin, J. Barrio, G. Peng, J. Tzadikov, L. Abisdris, M. Volokh and M. Shalom, *Nat. Commun.*, 2020, **11**, 4701.

9 L. Jiang, X. Yuan, Y. Pan, J. Liang, G. Zeng, Z. Wu and H. Wang, *Appl. Catal., B*, 2017, **217**, 388–406.

10 S. Mondal, G. Mark, L. Abisdris, J. Li, T. Shmila, J. Tzadikov, M. Volokh, L. Xing and M. Shalom, *Mater. Horiz.*, 2023, **10**, 1363–1372.

11 Y. Yang, S. Wang, Y. Jiao, Z. Wang, M. Xiao, A. Du, Y. Li, J. Wang and L. Wang, *Adv. Funct. Mater.*, 2018, **28**, 1805698.

12 S. Mondal, G. Mark, A. Tashakory, M. Volokh and M. Shalom, *J. Mater. Chem. A*, 2024, **12**, 11502–11510.

13 T. Shmila, S. Mondal, S. Barzilai, N. Karjule, M. Volokh and M. Shalom, *Small*, 2023, **19**, 2303602.

14 F. Li, X. Yue, Y. Liao, L. Qiao, K. Lv and Q. Xiang, *Nat. Commun.*, 2023, **14**, 3901.

15 N. Karjule, C. Singh, J. Barrio, J. Tzadikov, I. Liberman, M. Volokh, E. Palomares, I. Hod and M. Shalom, *Adv. Funct. Mater.*, 2021, **31**, 2101724.

16 Y. Hou, F. Zuo, A. P. Dagg, J. Liu and P. Feng, *Adv. Mater.*, 2014, **26**, 5043–5049.

17 W. Zhang, J. Albero, L. Xi, K. M. Lange, H. Garcia, X. Wang and M. Shalom, *ACS Appl. Mater. Interfaces*, 2017, **9**, 32667–32677.

18 R. Gong, D. Mitoraj, D. Gao, M. Mundszinger, D. Sorsche, U. Kaiser, C. Streb, R. Beranek and S. Rau, *Adv. Sustainable Syst.*, 2022, **6**, 2100473.

19 I. Cesar, A. Kay, J. A. Gonzalez Martinez and M. Grätzel, *J. Am. Chem. Soc.*, 2006, **128**, 4582–4583.

20 Z. Wang, Y. Gu, L. Zheng, J. Hou, H. Zheng, S. Sun and L. Wang, *Adv. Mater.*, 2022, **34**, 2106776.

21 J. Liu, Z. Luo, X. Mao, Y. Dong, L. Peng, D. Sun-Waterhouse, J. V Kennedy and G. I. N. Waterhouse, *Small*, 2022, **18**, 2204553.

22 B. Liu, X. Wang, Y. Zhang, L. Xu, T. Wang, X. Xiao, S. Wang, L. Wang and W. Huang, *Angew. Chem., Int. Ed.*, 2023, **62**, e202217346.

23 Z. Zhang, X. Huang, B. Zhang and Y. Bi, *Energy Environ. Sci.*, 2022, **15**, 2867–2873.

24 J. Lin, X. Han, S. Liu, Y. Lv, X. Li, Y. Zhao, Y. Li, L. Wang and S. Zhu, *Appl. Catal., B*, 2023, **320**, 121947.

25 A. Tashakory, N. Karjule, L. Abisdris, M. Volokh and M. Shalom, *Adv. Sustainable Syst.*, 2021, **5**, 2100005.

26 J. Xia, N. Karjule, L. Abisdris, M. Volokh and M. Shalom, *Chem. Mater.*, 2020, **32**, 5845–5853.

27 P. Garrido-Barros, C. Gimbert-Suriñach, R. Matheu, X. Sala and A. Llobet, *Chem. Soc. Rev.*, 2017, **46**, 6088–6098.

28 M. Gil-Sepulcre and A. Llobet, *Nat. Catal.*, 2022, **5**, 79–82.

29 N. Vereshchuk, M. Gil-Sepulcre, A. Ghaderian, J. Holub, C. Gimbert-Suriñach and A. Llobet, *Chem. Soc. Rev.*, 2023, **52**, 196–211.

30 R. Matheu, M. Z. Ertem, J. Benet-Buchholz, E. Coronado, V. S. Batista, X. Sala and A. Llobet, *J. Am. Chem. Soc.*, 2015, **137**, 10786–10795.

31 R. Matheu, I. A. Moreno-Hernandez, X. Sala, H. B. Gray, B. S. Brunschwig, A. Llobet and N. S. Lewis, *J. Am. Chem. Soc.*, 2017, **139**, 11345–11348.

32 J. Creus, R. Matheu, I. Peñafiel, D. Moonshiram, P. Blondeau, J. Benet-Buchholz, J. García-Antón, X. Sala, C. Godard and A. Llobet, *Angew. Chem., Int. Ed.*, 2016, **55**, 15382–15386.

33 S. Grau, S. Berardi, A. Moya, R. Matheu, V. Cristino, J. J. Vilatela, C. A. Bignozzi, S. Caramori, C. Gimbert-Suriñach and A. Llobet, *Sustainable Energy Fuels*, 2018, **2**, 1979–1985.

34 M. A. Hoque, M. Gil-Sepulcre, A. de Aguirre, J. A. A. W. Elemans, D. Moonshiram, R. Matheu, Y. Shi, J. Benet-Buchholz, X. Sala, M. Malfois, E. Solano, J. Lim, A. Garzón-Manjón, C. Scheu, M. Lanza, F. Maseras, C. Gimbert-Suriñach and A. Llobet, *Nat. Chem.*, 2020, **12**, 1060–1066.

35 M. Gil-Sepulcre, J. O. Lindner, D. Schindler, L. Velasco, D. Moonshiram, O. Rüdiger, S. DeBeer, V. Stepanenko, E. Solano, F. Würthner and A. Llobet, *J. Am. Chem. Soc.*, 2021, **143**, 11651–11661.

36 D. Schindler, M. Gil-Sepulcre, J. O. Lindner, V. Stepanenko, D. Moonshiram, A. Llobet and F. Würthner, *Adv. Energy Mater.*, 2020, **10**, 2002329.

37 R. S. Roy, S. Mondal, S. Mishra, M. Banoo, L. Sahoo, A. Kumar, C. P. Vinod, A. K. De and U. K. Gautam, *Appl. Catal., B*, 2023, **322**, 122069.

38 G. Mark, S. Mondal, M. Volokh, J. Xia and M. Shalom, *Sol. RRL*, 2022, **6**, 2200834.

39 S. Mondal, L. Sahoo, Y. Vaishnav, S. Mishra, R. S. Roy, C. P. Vinod, A. K. De and U. K. Gautam, *J. Mater. Chem. A*, 2020, **8**, 20581–20592.

40 N. Karjule, J. Barrio, L. Xing, M. Volokh and M. Shalom, *Nano Lett.*, 2020, **20**, 4618–4624.

41 Y. Hou, Y. Zhu, Y. Xu and X. Wang, *Appl. Catal., B*, 2014, **156–157**, 122–127.

42 Q. Zhang, X. Chen, Z. Yang, T. Yu, L. Liu and J. Ye, *ACS Appl. Mater. Interfaces*, 2022, **14**, 3970–3979.

43 M. K. Awasthi, R. K. Rai, S. Behrens and S. K. Singh, *Catal. Sci. Technol.*, 2021, **11**, 136–142.

44 J. Ma, X. Bai, W. He, S. Wang, L. Li, H. Chen, T. Wang, X. Zhang, Y. Li and L. Zhang, *Chem. Commun.*, 2019, **55**, 12567–12570.

45 M. Volokh and M. Shalom, *Ann. N. Y. Acad. Sci.*, 2023, **1521**, 5–13.

46 I. N. Cloward, T. Liu, J. Rose, T. Jurado, A. G. Bonn, M. B. Chambers, C. L. Pitman, M. A. Ter Horst and A. J. M. Miller, *Nat. Chem.*, 2024, 1–8.

47 G. Li, A. Yella, D. G. Brown, S. I. Gorelsky, M. K. Nazeeruddin, M. Grätzel, C. P. Berlinguette and M. Shatruk, *Inorg. Chem.*, 2014, **53**, 5417–5419.

48 M. Grätzel, *Acc. Chem. Res.*, 2009, **42**, 1788–1798.